Micromechanical testing and modelling of blast furnace slag cement pastes

Šavija, Branko; Zhang, Hongzhi; Schlangen, Erik

DOI
10.1016/j.conbuildmat.2019.117841

Publication date
2020

Document Version
Final published version

Published in
Construction and Building Materials

Construction and Building Materials 239 (2020) 117841

Contents lists available at ScienceDirect

Construction and Building Materials

journal homepage: www.elsevier.com/locate/conbuildmat

Micromechanical testing and modelling of blast furnace slag cement pastes

Branko Šavija, Hongzhi Zhang *, Erik Schlangen

Microlab, Delft University of Technology, Delft, Netherlands

HIGHLIGHTS

- Grayscale values from X-ray CT scans of slag pastes can be correlated with nanoindentation measurements of elastic modulus.
- A micromechanical model utilizing nanoindentation and X-ray computed tomography for slag cement paste is created.
- Advanced micromechanical experiments for estimating the micro-scale tensile strength and elastic modulus are performed.
- The presented work will form a basis for micromechanical testing and modelling of blended cement paste systems in the future.

ARTICLE INFO

Article history:
Received 13 August 2019
Received in revised form 17 October 2019
Accepted 10 December 2019

Keywords:
Lattice model
Nanoindentation
Micromechanics
Experimental testing

ABSTRACT

This work aims to understand deformation and fracture processes in blast furnace slag cement pastes made using CEM III/B which is commonly used in the Dutch infrastructure sector. First, based on our previous work on Portland cement pastes, a micromechanical model utilizing nanoindentation and X-ray computed tomography (CT) for input is created. Statistical analysis are carried out and shows that grayscale values from X-ray CT scans of slag pastes can be linearly correlated with nanoindentation measurements of elastic modulus. Simulations of uniaxial tension are then performed for varying w/c ratios using the Delft lattice model and microstructure obtained from X-ray CT. In addition, advanced micromechanical experiments for estimating the micro-scale tensile strength and elastic modulus are performed. Experimental and simulation results are then critically discussed and compared. It shows that simulation results match the measured tensile strength quite well although some discrepancy does exist at lower w/c ratios. In addition, the observations are compared to our previous findings on ordinary Portland cement pastes. It is found that tensile strength and elastic moduli of slag pastes at 28 days are higher than those of Portland cement pastes with the same w/c ratio. This study will form a basis for micromechanical testing and modelling of blended cement paste systems in the future.

1. Introduction

Concrete is the most widely used man made material in the world. Unfortunately, the production of Portland cement, the most common binder, is responsible for 5–7% of the total CO_2 anthropogenic emissions [1]. Since the widespread use of concrete is not expected to decrease in the near future, attention has been turned to alternative binders. Although numerous options for "cement-free" concrete – such as e.g. alkali activated materials [2] – have been proposed in recent years, it is at present much more common to replace a certain percentage of Portland cement in the mixture with an alternative material. These materials are known as supplementary cementitious materials (SCMs) [3,4]. Most commonly used SCMs are waste materials and/or byproducts of other industries, such as fly ash from coal used in power stations or blast furnace slag resulting from the steel manufacturing process. Apart from the environmental benefit, these SCMs can result in concrete mixtures with improved durability resulting from refinements in the pore structure [5]. On the other hand, concretes with SCMs can be more susceptible to cracking due to e.g. increased autogenous shrinkage [6] and have altered fracture behavior [7,8].

Deformation and fracture of heterogeneous porous materials depend on their pore structure, chemomechanical properties of solid phases and their spatial distribution [9]. Nevertheless, origins of deformation at fracture at micro- and nano-length scales of blended cement pastes remain scarcely explained. While numerous studies have been devoted to understanding strength of ordinary Portland cement (OPC) pastes (most notably

* Corresponding author.
E-mail address: h.zhang-5@tudelft.nl (H. Zhang).

https://doi.org/10.1016/j.conbuildmat.2019.117841
0950-0618/

nanoindentation [10–13] and micro-cantilever beam bending [14,15]), not a lot of attention has been devoted to blended binders. Wei et al. [16] used nanoindentation to measure the micromechanical properties of OPC/slag blended cement pastes. Although they observed unreacted slag particles to be somewhat stiffer than cement clinker particles, they reported that the indentation modulus and hardness of main hydration phases (low density and high-density C-S-H) are not altered by the partial slag replacement. Similar results were reported by Zadehi and Bobko [17]. On the other hand, Hu et al. [18] concluded that incorporating slag in the cementitious composites would lead to the changes in the physical properties of hydration products. It should be noted that it has been reported that Ca/Si ratio of the C-S-H does have an effect on the micromechanical properties of C-S-H: namely, the lower the Ca/Si ratio, the higher the elastic modulus [19]. Furthermore, Hu et al. [20,21] measured the micromechanical properties of each phases in fly ash blended cement pastes and concluded that two types of fly ash parties with significantly differing mechanical properties and chemical compositions can be observed. However, Wilson et al.[22] suggested that the main contribution of SCMs was on the kind and the spatial distribution of the hydration products instead. These findings suggest that many different factors need to be considered for prediction of mechanical properties of cement paste containing SCMs such as slag.

In order to predict the elastic and fracture properties for a complex heterogeneous of hardened cement paste, modelling approaches informed by advanced micromechanical characterizations such as nanoindentation [13,23] have been developed in recent years. Most approaches fall into two categories: continuum micromechanics [24,25] or discrete (lattice) approaches [26,27]. In addition, phase field models have been proposed very recently [28,29]. It is quite surprising that micromechanical models of cement paste considering supplementary cementitious materials are quite rare. Hlobil et al. [30] proposed a four-scale micromechanical model for compressive strength of blended cement paste. A time dependent model able to simulate the time evolution of Young's modulus and compressive strength of blended cementitious materials was proposed by Lavergne et al. [31]. This is possibly related to the following: most common models for simulating hydration of cement paste, such as μic [32] and Hymostruc3D [33], are limited to hydration of Portland cement paste. Note that a recent extension of the Hymostruc3D model [34] does allow for simulating hydration of blended cementitious systems. However, this has not been used as input for micromechanical simulations to date. Since these models are commonly used for creating input for micromechanical simulations, this is a clear limitation. Nevertheless, there is a clear need for more thorough understanding of micromechanical behavior of blended cement pastes. These models should be also experimentally validated at the appropriate length scale.

At Delft University of Technology, recently an approach for simulating micromechanical properties of hydrated cement paste based on coupling between X-ray computed tomography (CT) and nanoindentation has been developed [35]. The proposed approach takes advantage of the fact that the results of both techniques – i.e. grayscale values and elastic moduli from the X-ray CT and nanoindentation, respectively – depend on the density of the material. In addition, micro-scale testing techniques that enable directly measuring the micromechanical properties of hardened cement paste at the same scale at which the models are used (i.e. the micro-scale) have been developed. With these techniques, it is possible to directly measure the Young's modulus [36] and the splitting strength of micro-scale specimens of hardened cement paste [37–39]. In this work, the proposed modelling approach is extended on simulating deformation and fracture of hardened cement paste made using CEM III/B, with a high content (66–80%) of blast furnace slag. Furthermore, micromechanical tests were performed on specimens created using the same materials to validate the modelling approach. The findings are critically discussed in the view of our previous observations on OPC pastes. This study can form a basis for understanding of deformation and fracture of blended cement pastes. Furthermore, the approaches developed herein can be used in the future for tailoring of the micromechanical properties of cement-based materials.

2. Experimental

2.1. Materials

Cement paste specimens with different water to cement (w/c) ratios (0.3, 0.4, and 0.5) were prepared for the experimental part of the study. The materials used were CEM III/B 42.5 N LH (produced by ENCI B.V. Maastricht, Netherlands) and deionized water. The chemical composition of the cement (as provided by the manufacturer) is given in Table 1. Cement paste specimens were prepared in accordance with the EN 196-3:2005 + A1:2008 (E) standard. For mixing, a Hobart mixer was used. The mixing procedure was as follows: first, the cement was placed in the bowl; then, within 10 s, water was added. The mixture was then mixed for 90 s at low speed. The mixing was then stopped for 30 s while paste adhering to the mixer walls was scrapped off and added to the mixture. This was followed by additional 90 s of mixing. Total mixing time was therefore around 3 min. The fresh mixture was then cast into plastic cylindrical cups (34 mm diameter, 58 mm height), which were sealed and rotated for 24 h to avoid bleeding. The specimens were then cured in sealed conditions until reaching the age of 28 days. After 28 days, the specimens were demoulded and cut into 2 mm thick discs using a diamond precision saw. The slices were then used for preparing all specimens, as further described below. Hydration of the slices was stopped using solvent exchange by isopropanol [40]. The slices were immersed and taken out of the solution in total five times for a period of 1 min. Afterwards, the specimens were stored in isopropanol until testing. Prior to testing, the solvent was removed by evaporation at ambient conditions.

2.2. Micro-scale specimen preparation

Two different micro-scale specimen types were prepared for pastes of each w/c ratio: micro-cube specimens for micro-splitting tests, and micro-beam specimens for X-ray computed tomography and micro-beam bending tests. The following steps are performed in specimen preparation. The first step is to grind the thickness of the cement paste slice down to a desired thickness (100 μm and 500 μm for micro-cubes and micro-beams, respectively). A "Struers SystemAbele Accessories" apparatus was used for grinding and polishing of the paste specimens. The slice was

Table 1
Composition of the blast furnace slag cement used in the study and the ordinary Portland cement used in previous studies (% by mass).

Oxide	CEM III/B 42.5 N LH	CEM I 42.5 N
CaO	46.08	64.4
SiO_2	29.12	20.36
Al_2O_3	10.5	4.96
Fe_2O_3	1.32	3.17
K_2O	0.49	0.64
Na_2O	0.33	0.14
SO_3	3.01	2.57
MgO	7.47	2.09
TiO_2	0.81	/
Mn_3O_4	0.24	/
P_2O_5	0.21	0.18

mounted on a glass substrate using a UV glue and then ground down to 1 mm using a diamond ring grinding discs with grit size of 125 μm to 30 μm in descending order. Afterwards, the slice was turned around and the grinding procedure was continued until the required thickness was reached. The second step entails cutting of the micro-scale specimens from the prepared thin slice. This was done using a micro-dicing saw "MicroAce Series 3" (Loadpoint Ltd., Swindon, UK) over the thin section, as schematically shown in Fig. 1. For creating the micro-cubes, the dice was run in two perpendicular directions. For micro-beams, dicing was performed in 1 direction. Micro-cube specimens were left bonded to the substrate, while micro-beam specimens were debonded using acetone.

2.3. X-ray computed tomography

For each w/c ratio, one micro-beam specimen (500 × 500 μm) was used for X-ray computed tomography scanning. Micro-beams were clamped on a holder (Fig. 2) which was then placed in the chamber of the CT scanner (Phoenix Nanotom, Universal Systems, Manchester, UK). X-ray source tube was set as 120 kev/60 μA during scanning. 2800 images with an exposure time of 6 s were acquired on a GE DXR digital detector. The voxel resolution under these conditions was 2 × 2 × 2 μm^3/voxel. Although this resolution is not as high as others reported [29,41], it is sufficient to model the fracture behavior of hardened cement paste at micro-scale and consider its heterogeneity [37,42–44]. Reconstructed slices were carried out with Phoenix Datos|x software and a 3D stack of 8-bit cross-section images were generated in the end. A cubic region of interest (ROI) with a length of 200 μm was extracted from the specimen for the statistical analysis (see Fig. 3). To diminish the influence of beam hardening in the XCT experiment, the middle region of the specimen was chosen and analyzed.

2.4. Nanoindentation

For nanoindentation, the specimens of each w/c ratio were prepared as well. First, they were ground and polished to prepare a smooth surface. Ethanol was used as a cooling liquid instead of water in order to avoid further hydration. After grinding, each of the samples was polished with 6 μm (5 min), 3 μm (5 min), 1 μm (5 min) and 0.25 μm (25 min) diamond paste on a lapping table [45]. The samples were cleaned using an ultrasonic bath between consecutive polishing steps to remove any paste residue from the surface.

For nanoindentation testing, KLA-Tencor G200 (KLA, Milpitas, CA, USA) equipped with a Berkovich diamond tip was used. Prior to nanoindentation testing, a quartz standard was indented for calibration. The indentation depth was set to 1000 nm. Per specimen, 1000 indents were performed, always keeping the spacing between them >20 μm. The Continuous Stiffness Method (CSM) of Oliver and Pharr [46] was used to analyze the measurements. The CSM allows for a continuous measurement of contact stiffness as a function of indentation depth. Since nanoindentation actually measures the mechanical properties of the interaction volume around the indent (estimated as 3–5 h_{max}, h_{max} being the maximum indentation depth [47]), this allows for adjusting the interaction volume to correspond to the voxel size of X-ray CT (as described in detail in our previous work [35]). A similar approach has been proposed by others for correlating the nanomechanical measurements and chemical composition determined by WDS (wavelength dispersive spectroscopy) [48,49] and recently extended to nanoindentation [50]. Since the resolution of the X-ray CT was set to 2 μm^3, the E moduli for each indent were calculated in the range between 400 and 660 nm indentation depth. Poisson's ratio was kept constant at 0.18 throughout the analysis with the CSM method.

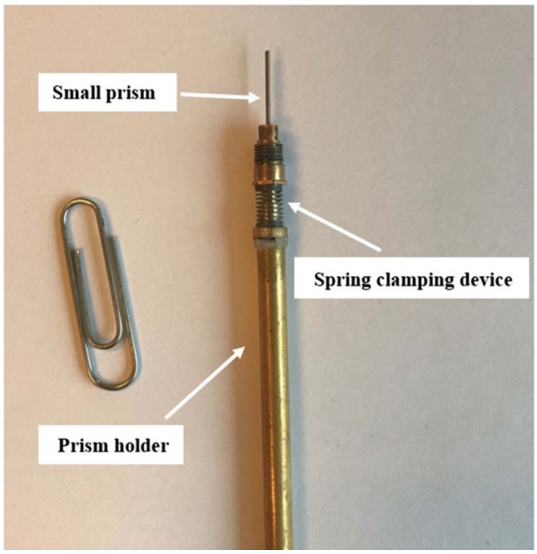

Fig. 2. A micro-beam clamped on a custom-made holder, prior to X-ray CT scanning.

2.5. Correlation between X-ray CT and nanoindentation measurements

X-ray CT provides grayscale value plots of the scanned microstructure in which the grey scale value (GSV) of each individual voxel is a function of the density and the atomic number [51]. Similarly, the density is related to the mechanical properties measured by nanoindentation [52]. In our previous work, it was shown that the histograms of nanoindentation measurement of elastic

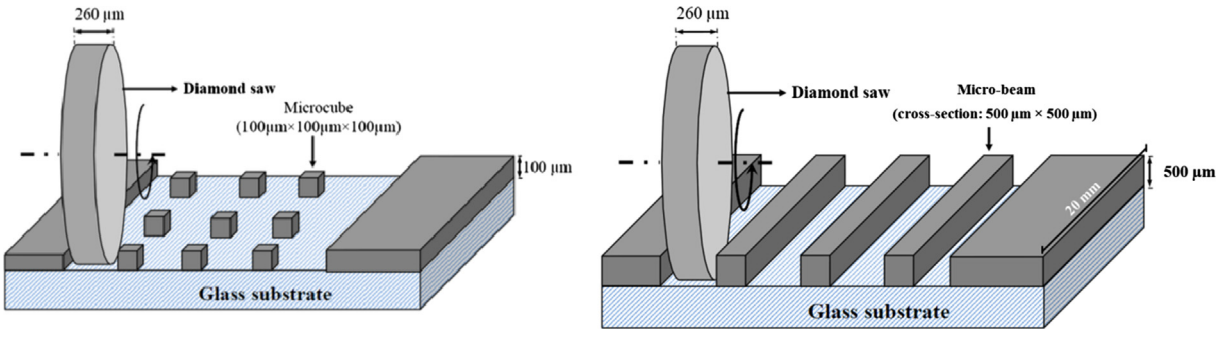

Fig. 1. Schematic description of the specimen preparation procedure: (Left) micro-cube preparation; (right) micro-beam preparation.

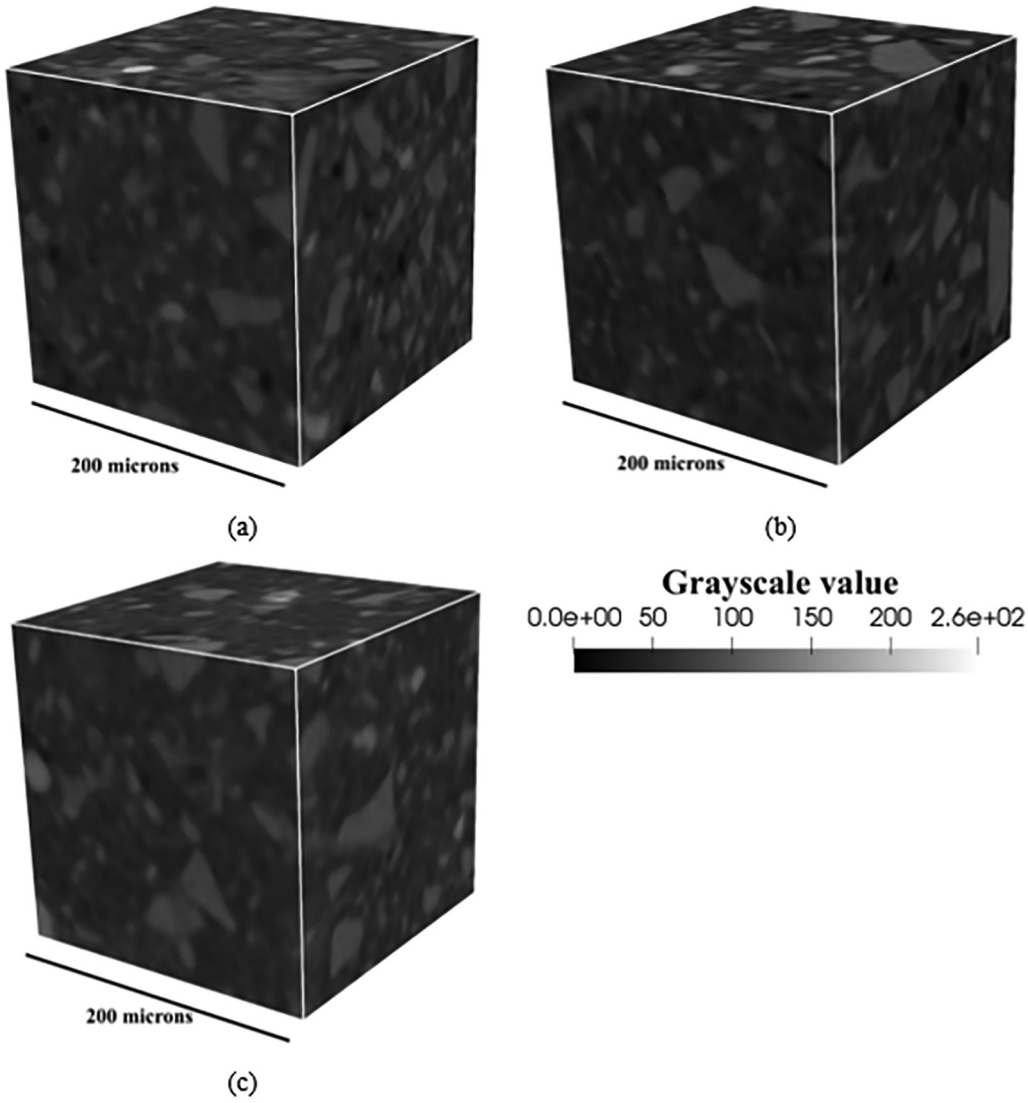

Fig. 3. Reconstructed microstructures of different w/c ratios: (a) 0.3; (b) 0.4 and (c) 0.5. Sub-volumes of 200x200x200 μm are shown.

moduli and grayscale values resulting from X-ray CT can be correlated [35]. Based on findings from the previous study, herein also a linear relationship between the elastic modulus (from nanoindentation) and the grayscale value (from X-ray CT) was adopted. To test whether this approach is valid also for the specimens used in the current study, a two-sample Kolmogorov-Smirnov (K-S) test was performed for each w/c ratio. This test quantifies the distance between the cumulative distribution functions of two samples [53]. The null hypothesis of this test states that the samples are drawn from the same distribution. For two one-dimensional probability density functions (PDFs), the K-S statistic can be written as:

$$D_{n,m} = \sup[F_{1,n}(x) - F_{2,m}(x)] \quad (1)$$

In Eq. (1), $F_{1,n}$ and $F_{2,m}$ are empirical distribution functions of the first and the second sample, respectively, while sup is the supremum function. The null hypothesis is rejected at the level α if the following holds:

$$D_{n,m} > c(\alpha)\sqrt{\frac{n+m}{nm}} \quad (2)$$

In Eq. (2), n and m are the sizes of the first and the second sample, respectively. The value of $c(\alpha)$ can be determined as [54]:

$$c(\alpha) = \sqrt{-\frac{1}{2}ln\left(\frac{\alpha}{2}\right)} \quad (3)$$

In Fig. 3, reconstructed X-ray CT microstructures for different w/c ratios are given. The image consists of 256 (0–255) levels of GSV that correspond to different densities of the components. In general, low density corresponds to a low GSV which is shown in black (i.e. pore), while high density leads to a high GSV which is shown in white. From Fig. 3, it is possible to observe some features of pore space (black), and unhydrated cement grains (grey). However, for the hydration products, as they have similar densities, it is difficult to be distinguished. Fig. 4 shows histograms of grayscale values and elastic moduli for the 3 tested w/c ratios. Histograms from two measurements are comparable and similar trend is observed. The first peak shifts to the left with the increasing of w/c ratio. This means that the specimens having higher w/c ratio have lower density components with lower elastic modulus.

Fig. 5 left shows linearly normalized PDFs of the two functions for each w/c ratio, while Fig. 5 right shows their cumulative probability functions. The following needs to be emphasized [35]: Young's modulus of a porous material such as cement paste approaches zero for porosity values lower than 100%; therefore, a critical porosity lower than 100% exists below which the measured

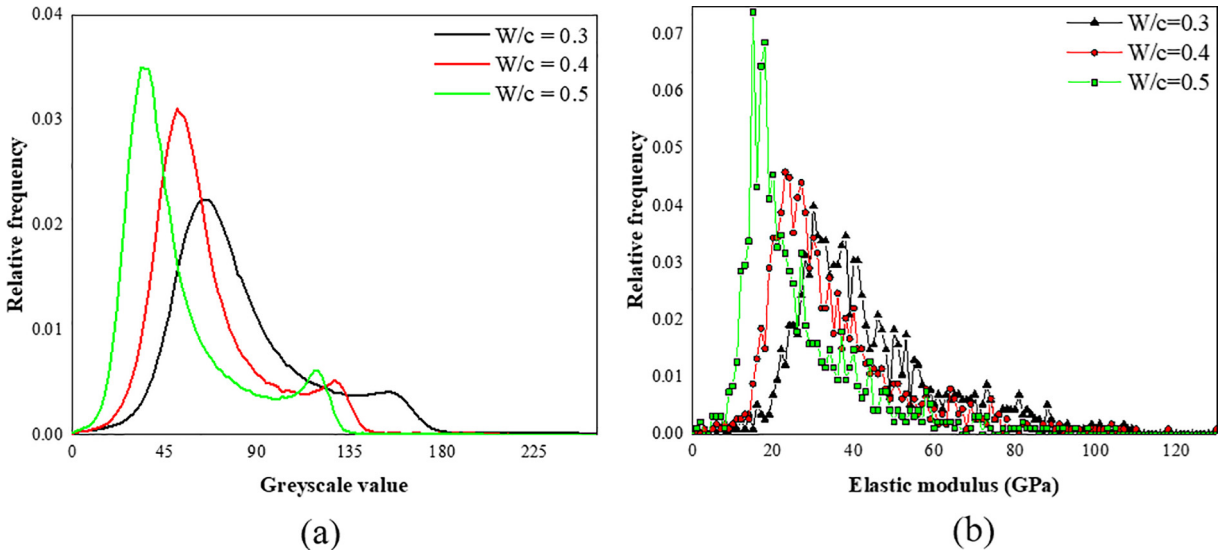

Fig. 4. Histograms of (a) GSV and (b) elastic modulus measured by nanoindentation for the three w/c ratios.

Young's modulus is zero. This means that, at a certain level of porosity (lower than 100%), the material within the volume is not able to sustain any load and therefore has a Young's modulus of 0 [55]. In X-ray CT can detect the voxels with porosity higher than this critical value. For example, an air voxel with 100% porosity has a GSV of 0. In nanoindentation testing, a microvolume with a zero stiffness cannot be tested. Therefore, to make the PDFs comparable, voxels with a porosity higher than critical (i.e. those that could not be tested using nanoindentation) had to be removed from the PDFs of the X-ray CT grayscale values. Therefore, a greyscale level (left tail) having the same probability as the detectable stiffness was selected and removed from the PDF (Tg = 42, 28 and 55 for w/c ratio 0.3, 0.4 and 0.5 respectively), and voxels with a lower GSV have been removed from the PDF. As a result, the minimum GSV has the same probability as the minimum detected indentation (Young's) modulus. Since this is dependent on the bin size, it was selected as 1 GPa and kept constant for all specimens.

For the selected parameters from Eq. (2), $n = 100^3$ (number of voxels in the ROI) and m = 1000 (number of indents). For a selected confidence interval of 95% (α = 0.05), Eq. (3) results in $c(\alpha)$ = 1.3581. Consequently, $D_{n,m} > 0.043$ is the condition for rejecting the null hypothesis (Eq. (2)). Values for the 3 tested w/c ratios are given in Table 2.

From Table 2, it can be seen that, according to Eq. (2), the null hypothesis cannot be rejected for any of the tested paste mixtures. This means that, in all cases, the two samples (i.e. indentation modulus and GSV of X-ray CT) are drawn from the same distribution with a 95% confidence level. This allows us to "map" the elastic modulus values to various GSV values. For a specific GSV of an individual voxel, its Young's modulus can be assigned according to the following equation [35]:

$$E_{local} = \min(F(x)) + (\max(F(x)) - \min(F(x))) \frac{GSV - T_g}{(255 - T_g)} \quad (4)$$

In Eq. (4), T_g is the threshold GSV, below which the voxel would have a zero measurable indentation modulus (values of T_g are 42, 28 and 55 for w/c ratio 0.3, 0.4 and 0.5 respectively). Min($F(x)$) and max($F(x)$) are the minimum and maximum values in the indentation modulus histogram (1 and 120 GPa, respectively).

On the other hand, it has been shown in our previous work [35] that PDF of the indentation hardness cannot be correlated with the GSV. In our previous work, however, it was shown that there is a power relationship between indentation hardness and elastic modulus in a form of $H_{local} = aE^b_{local}$ (Fig. 6). A similar relationship between hardness and elastic modulus has been proposed for alumina porcelain in the past [56]. Furthermore, the ratio between hardness and tensile strength varies between 3 and 183 for different materials [57]. For cement paste, this ratio is found to be around 12 by the authors [39]. Using this linear relationship, satisfactory modelling results which are comparable with experiments can be obtained [37,42,44,58]. Therefore, it is adopted in the current study. Furthermore, a has been proposed in the past [26]. Therefore, for the numerical simulations performed in this work, tensile strength of individual voxels was considered to have a power relationship with the elastic modulus as follows [35]:

$$f_{t,local} = \frac{aE^b_{local}}{12} \quad (5)$$

In Eq. (5), a and b are empirical fitting parameters, obtained as a = 0.00352 and b = 1.739, see Fig. 6.

2.6. Modelling of deformation and fracture

In this work, the Delft lattice model [59,60] was used to simulate deformation and fracture of blended cement pastes. The model has been used for simulating cracking in cementitious and other quasi-brittle materials under various external [61,62] and internal loads [63,64]. In the model, the continuum is discretized as a set of beam elements that can transfer forces. Typically, each lattice beam has elastic-perfectly brittle behavior [65]. To simulate cracking, a set of linear elastic analyses is performed. In each analysis step, a beam element with a highest stress to strength ratio is identified and removed from the lattice mesh, signifying the occurrence of a small crack. This is followed by a new linear elastic analysis in which the same procedure is performed. This is repeated until a predefined criterion (e.g. external load or displacement) is reached.

In the current study, sub-volumes of 100 × 100 × 100 μm with a 2 μm^3 resolution were extracted from X-ray CT images of each w/c ratio. Each voxel was assigned with a Young's modulus and a tensile strength according to its GSV and Eqs. (4) and (5).

In each voxel, a virtual cell was defined (see Fig. 7). In each cell, a node is randomly placed. The ratio between cell and voxel size defines the randomness of the mesh. A random mesh reduces crack

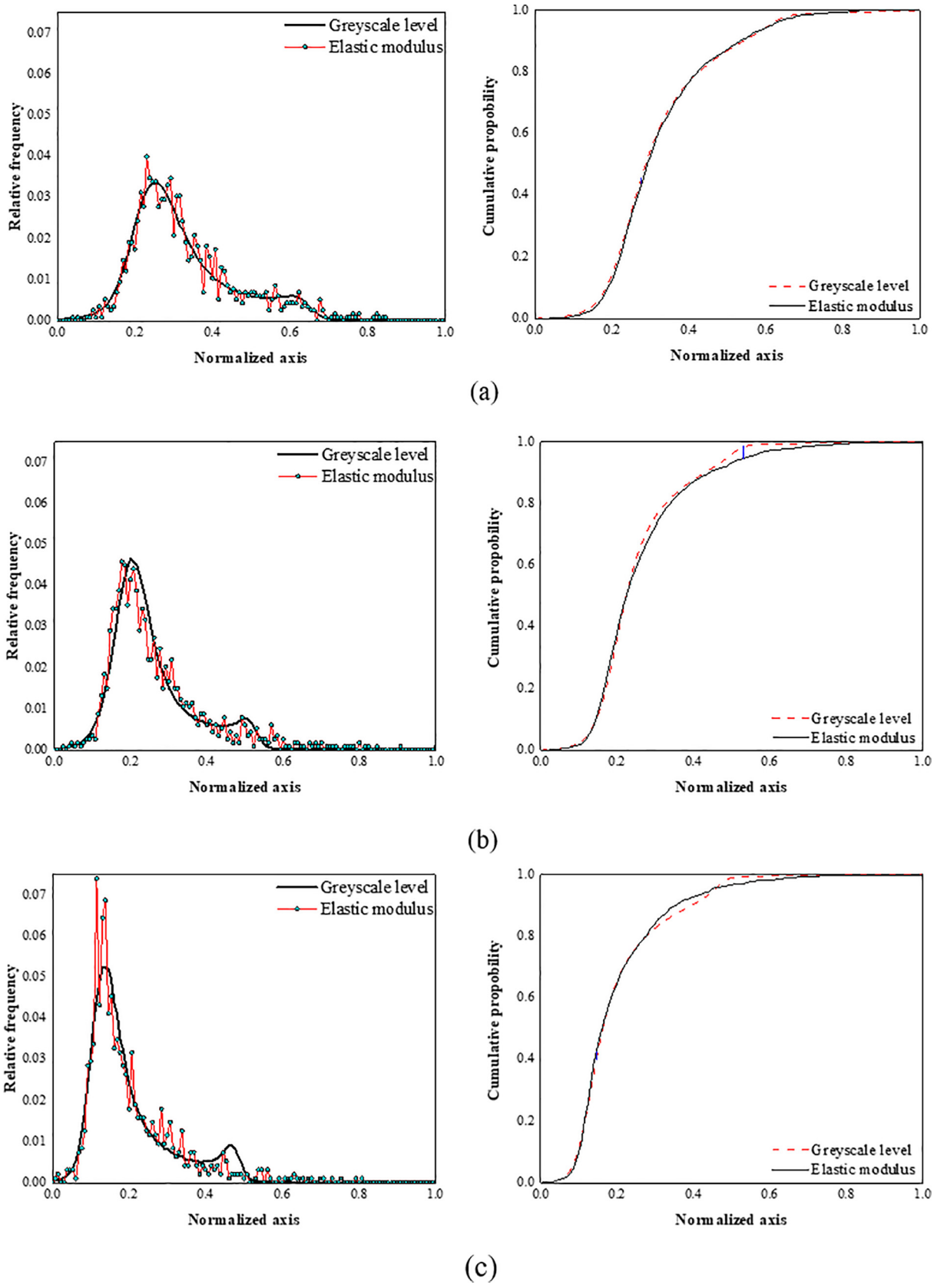

Fig. 5. Comparison of distributions of Young's modulus and greyscale levels with normalized axis for the 3 tested w/c ratios: (a) w/c = 0.3; (b) w/c = 0.4; (c)w/c = 0.5 (left: histogram of the two distributions; right: cumulative probability of the two distributions).

Table 2
K-S statistic parameter for all tested mixtures.

W/c	$D_{n,m}$
0.3	0.0213
0.4	0.0380
0.5	0.0359

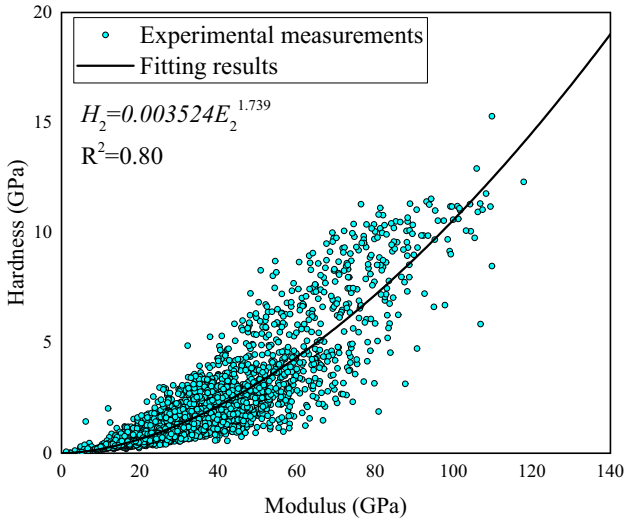

Fig. 6. Relationship between hardness and Young's modulus from nanoindentation.

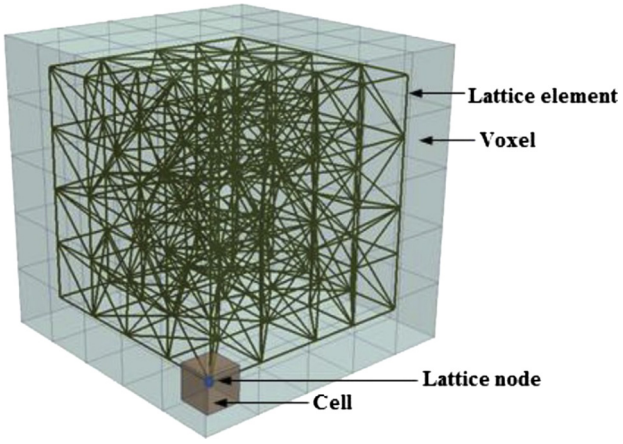

Fig. 7. Schematic view of lattice mesh construction of a cubic volume of 5 × 5 × 5 voxels.

directionality in numerical simulations. Herein, a randomness of 0.5 is selected. A Delaunay triangulation is then performed on the set of nodes to create the lattice mesh, as explained by Yip et al. [66]. For each lattice element, the Young's modulus was assigned as the harmonic average of the two connected voxels, while tensile strength was taken as the lowest value of the two connecting voxels (see Fig. 11 left). Elements with either node positioned in a voxel with GSV lower than T_g were removed from the mesh.

A simulated uniaxial tensile test was performed on each lattice microstructure. One side was subjected to prescribed displacement, while the opposite side was completely restrained. This allowed for determining the uniaxial tensile strength and the elastic modulus of pastes with different w/c ratios.

2.7. Micromechanical testing

Two types of micromechanical tests, previously developed by the authors, have been employed to determine the micromechanical properties of slag hydrated cement pastes. The purpose of this testing was two-fold: first, although boundary and loading conditions are different compared to the simulations, the tests were used to validate the modelling results. Second, the test results are compared to previously obtained measurements on OPC pastes.

The first test performed was the so-called one-sided micro-cube splitting [37,38]. For this test, and array of micro-cubes (as shown in Fig. 1 left) is used. Testing was performed using the nanoindenter (same apparatus as described in section 2.4, see Fig. 8). The Berkovich tip was replaced with a cylindrical wedge tip (radius 9.6 μm, length 200 μm) in order to apply a splitting line load across the midsection of the micro-cube. Experiments were run in displacement control with a rate of 50 nm/s.

The second test was three-point bending of micro-beam specimens [36]. In this test, beam specimens with a cross section of 500 × 500 μm (obtained as shown in Fig. 1 right) were subjected to three-point bending. This test was also performed in the nanoindenter using a cylindrical wedge tip (radius 9.6 μm, length 700 μm) instead of the Berkovich tip. The micro-beams were placed on a 3D-printed plastic support with a span of 12 mm (Fig. 9). This length is much larger than the length of the cross-section to minimize the influence of shear on the measured flexure strength. Line load was applied in the middle-span of the beam through the tip. Experiments were run in displacement control with a rate of 500 nm/s. The load and displacement responses were recorded by the indenter automatically.

3. Results and discussion

3.1. Modelling results

Curves from simulated uniaxial tensile tests on slag pastes with different w/c ratios are given in Fig. 10. From the simulation output, several quantities can be directly determined: the elastic modulus, the tensile strength, and the fracture energy. Herein, fracture energy is calculated as the area below the post-peak part of the stress/displacement curve. Simulation results are summarized in Table 3. As expected, the Young's modulus and the tensile strength decrease with the increasing w/c ratio. This does not hold for the fracture energy, since it can be seen that the fracture energy of the specimen with w/c of 0.4 is higher than that of the specimen with 0.3. The fracture energy depends, mathematically, on two factors: the peak load and the behavior after the post peak (with the more brittle behavior resulting in lower fracture energy and vice versa). The specimen with w/c = 0.4 shows a somewhat more ductile behavior compared to the one with w/c = 0.3, resulting in higher fracture energy despite the lower peak strength. Following the approach proposed in [36,37,67], these simulated stress–strain curves can be further used as input for the *meso*-scale models.

It can be also observed that the simulation results show somewhat higher strength of slag cement paste compared to the Portland cement paste of the same w/c ratio (reported in our previous work [35]. This is somewhat unexpected, as available experiments on the mm to cm length scale show higher (compressive) strength of OPC pastes compared to pastes with high slag contents [68–70]. This could be caused by the refinement of the capillary porosity caused by the hydraulic reactions of slag, since it is known that (tensile) strength is inversely proportional to porosity [71]. An inversely proportional relationship between porosity and elastic modulus has also been reported [43]. A comparison between experimental measurements is given later.

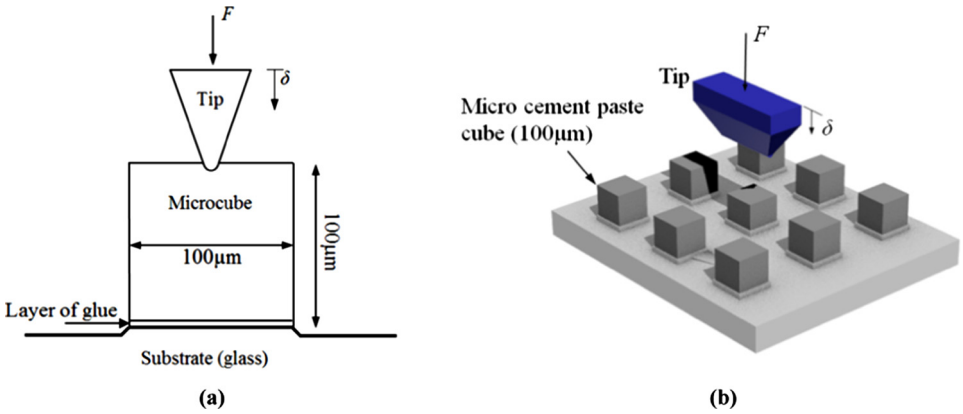

Fig. 8. Schematic description of: (a) loading procedure of an individual micro-cube; (b) testing of an array of micro-cubes.

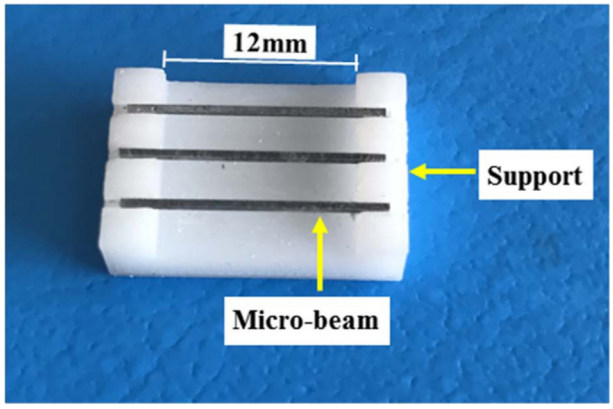

Fig. 9. Micro-beam specimens placed on a 3D-printed support.

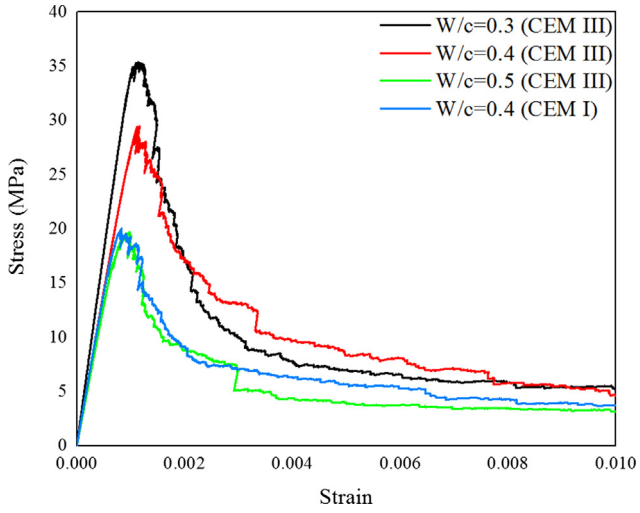

Fig. 10. Results of the uniaxial tensile test simulations of slag cement pastes with different w/c ratios. For comparison, a simulation result from our previous work on OPC is given [35].

Fig. 11 shows crack propagation in slag pastes of different w/c ratios. For all 3 simulated microstructures, it can be seen that cracking in general occurs in "softer" parts of the microstructure, and the cracks tend to occur around the stiff areas (i.e. those corresponding to unhydrated cement and/or unreacted slag particles). This is similar to the behavior observed at the macro (i.e. concrete) level, where it has been observed that, in general, cracking propagates through the matrix and around stiff aggregate particles, although this is aided by the presence of the weak interfacial transition zone around the aggregates [72]. Furthermore, similar behavior has been reported to occur in Portland cement paste due to presence of unhydrated cement particles [26]. At the peak load, already some cracks form: afterwards, these cracks tend to grow and coalesce, leading to failure of the (simulated) specimen.

3.2. Experimental results

For each w/c ratio, 35 micro-cubes were tested in one sided splitting. Similar to our previous work on Portland cement paste [37], it was observed that the tensile strength results show a lot of scatter due to the heterogeneous nature of the slag cement paste at this length scale. Therefore, the results were analyzed with Weibull statistics. In the absence of specific requirements, a general rule-of-thumb is that approximately 30 test specimens provide adequate Weibull strength distribution parameters, with more test specimens contributing little towards better uncertainty estimates [73]. The probability of failure P_f can be expressed through the following relation [74]:

$$P_f = 1 - exp\left[-\left(\frac{\sigma}{\sigma_0}\right)^m\right] \quad (6)$$

In Eq. (6), parameter m is called the Weibull modulus and σ_0 the scaling parameter equal to the stress corresponding to 63% probability of failure. Fig. 12 shows plots of splitting tensile strength for slag cement pastes with different w/c ratios in the Weibull coordinate system. In general, a good linear fit is observed with a $R^2 > 0.9$. m is the slope of the fit and σ_0 can be calculated from the x-intercept of this fit. It is worth mentioning that if the strengths have an infinite scatter, the fitted line in Fig. 12 would be vertical and m would approach zero. Conversely, a Weibull modulus approaching infinity would correspond to a group with specimens have exactly the same strength with each other and a horizontal line can be expected in Fig. 12 for this case. A summary of experimental results and parameters is given in Table 4. Similar to the Portland cement paste, the Weibull modulus and the scaling factor decrease with the increase of the w/c ratio. This essentially means that slag cement pastes with a lower w/c ratio have a higher and less variable splitting strength. The same was observed for ordinary Portland cement pastes in our previous work [37]. Furthermore, it can be seen that, on average, slag pastes with the same w/c ratio have a higher splitting strength compared to the ordinary Portland cement pastes at 28 days.

Table 3
Simulated micromechanical properties of slag cement pastes with different w/c ratios. For comparison, a simulation result from our previous work on OPC is given [35].

w/c	Young's modulus (GPa)	Tensile strength (MPa)	Strain at peak (%)	Fracture energy (J/m^2)
0.3	35.89	35.36	0.114	7.97
0.4	28.54	29.45	0.116	8.65
0.4 (OPC) [35]	28.53	20.01	0.083	5.89
0.5	25.93	19.68	0.099	4.67

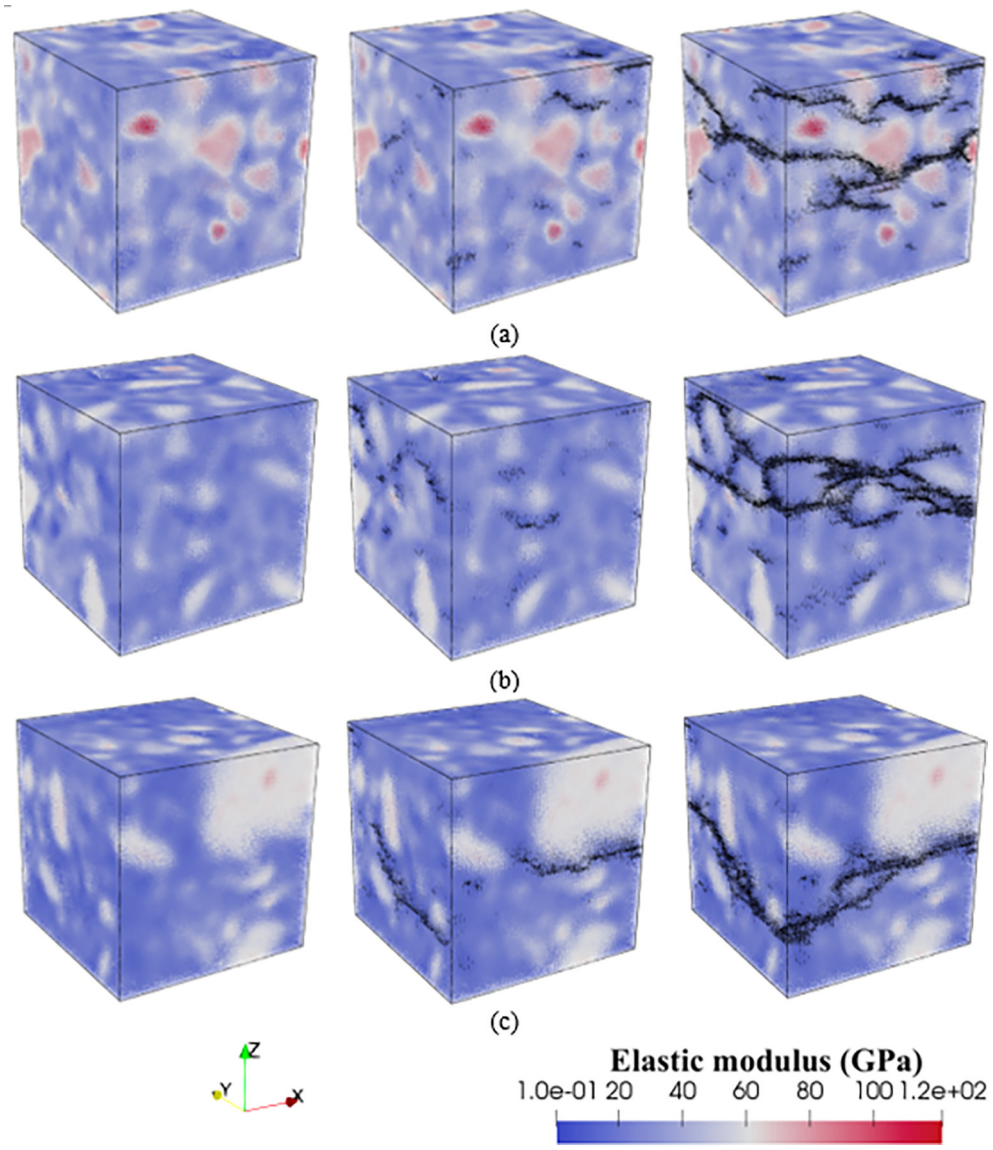

Fig. 11. (left) Microstructures used as input for uniaxial tension simulations showing gradients of elastic modulus; (middle) cracks at peak load; (right) cracks at failure for (a) slag paste with w/c = 0.3; (b) slag paste with w/c = 0.4; and (c) slag paste with w/c = 0.5 (black is used to present crack).

A comparison between simulated and measured uniaxial tensile strengths is shown in Fig. 13. Clearly, the simulated uniaxial tensile strengths are somewhat higher than the measured values for lower w/c ratios (0.3 and 0.4), while they correspond quite well for the w/c = 0.5. There could be several reasons for this discrepancy. First, only one simulation was performed for each w/c ratio, and it is possible that the selected microstructure was somewhat higher than the average. In general, it is recommended to treat the fracture behavior of cement paste in a stochastic way due to its heterogeneous nature [42]. Since this requires significant computational effort, it was not done in the present study. The second reason for the discrepancy could be the proposed relationship between indentation modulus and the tensile strength used in this study (Eq. (5)). Although unreacted slag particles are somewhat stiffer compared to other phases in the paste, it is possible that their contribution to the tensile strength is lower. The somewhat lower R^2 value for the fit between hardness and the elastic modulus (0.8, see Fig. 6) could be an indication for this. Nevertheless, the simulated results show reasonable agreement with the experimental data.

In addition, micro-beam three-point bending tests have been performed as described in section 2.7. For each w/c ratio, 10

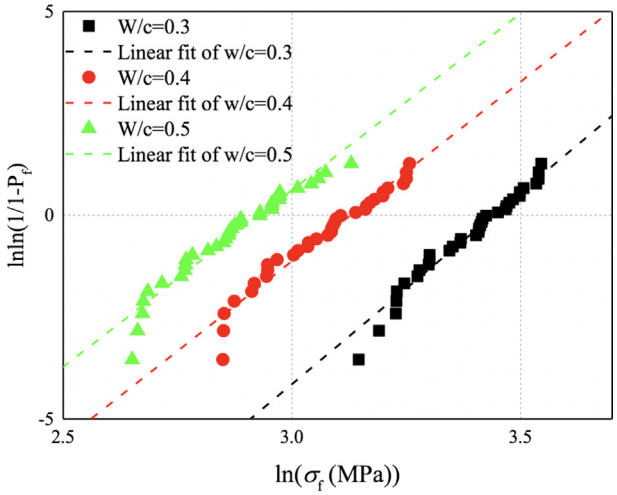

Fig. 12. Weibull plots for measured tensile strength of slag cement pastes with different w/c ratios.

micro-beam specimens were fabricated and tested. Fig. 14 shows measured load–displacement curves for all micro-beam specimens. The load first increases monotonically with the displacement until reaches a critical load. Afterwards, a displacement jump is observed, leading to a plateau in the end of the curve. It must be emphasized that the plateau in the curves does not correspond to the material behavior, but a catastrophic failure of the specimen. This is because the control of the nanoindenter is not fast enough to enable a measurement of the post-peak behavior.

From the micro-beam specimen tests, and based on Euler-Bernoulli beam theory, the flexural strength and the Young's modulus can be derived. The values are given in Table 5. Again, it can be seen that, for the same w/c ratio, slag pastes show higher stiffness and higher flexural strength compared to the ordinary Portland cement pastes at 28 days. The reason is probably, again, the finer pore structure of slag pastes compared to OPC pastes.

By comparing strength values from Tables 4 and 5 it can be seen that micro-beam tests show lower flexural (tensile) strength compared to micro-cube splitting tests. As shown in our previous work [36], this is because of size effect: micro-beam specimens are significantly larger than micro-cube specimens and can be considered as "sub-meso" scale. As such, they comprise possibly pores larger than micro-cube specimen size, and expectedly have lower strength. The trend, however, is as expected: an increase in w/c ratio leads to a decrease in flexural strength. For the same w/c ratio, slag specimens show higher strength compared to Portland cement paste specimens. This is the same behavior observed in micro-cube splitting.

Young's modulus also shows an inversely proportional relationship with the w/c ratio. Furthermore, measured moduli are always higher for slag pastes compared to Portland cement pastes for the same w/c ratio. However, it is noticeable that measured values are lower than simulated values (Fig. 15), although the trend is the same which is signified by almost parallel lines in Fig. 15. As shown in our previous work [36], this is probably because the displacement is not the actual displacement of the micro-beam, but of the loading indenter. It therefore includes, apart from the actual displacement, other secondary effects as well: most notably, local imprinting of the nanoindenter into the micro-beams, and possible settlement of the supports during testing. Consequently, a similar discrepancy in terms of absolute values has been observed for ordinary Portland cement pastes in our previous work (Fig. 15). Nevertheless, the measurement is able to capture the general trend of decreasing modulus with increasing w/c ratios for both slag and OPC pastes.

3.3. General discussion

As shown previously, paste specimens made using CEM III/B showed (in both numerical simulations and experiments) a somewhat higher strength compared to OPC paste specimens with the same w/c ratio. This seems not to be in accordance with (limited) experimental data, as explained already. Here, a possible explanation is sought.

It is known that strength and stiffness of cement paste are inversely proportional to porosity [75]. Therefore, refinement of the pore structure caused by the hydraulic reaction of blast furnace slag could be a cause of the discrepancy. Therefore, X-ray CT images were used to obtain the total capillary porosity for all examined cement paste samples, i.e. CEM III/B pastes used in the current study as well as CEM I samples from previous studies. For segmenting the capillary porosity, the so-called tangent-slope method [39,76] (illustrated in Fig. 16) was applied on the

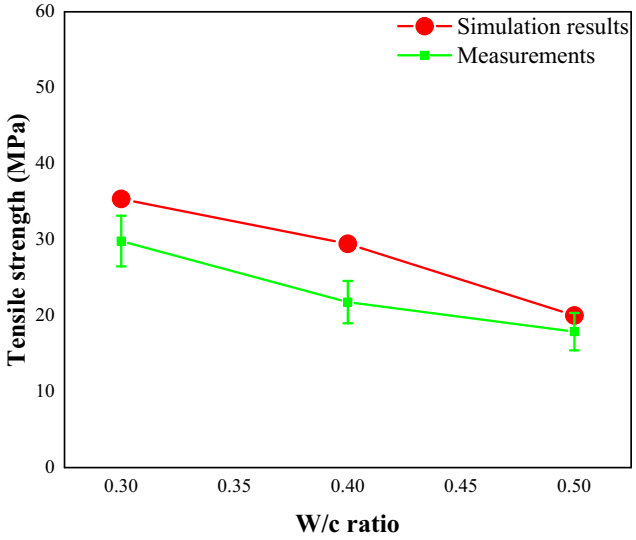

Fig. 13. A comparison between simulated and measured tensile strengths of slag pastes with different w/c ratios (error bars indicate standard deviation).

Table 4
Splitting strength and Weibull parameters for tested mixtures. For comparison, result of Portland cement paste specimens from our previous work are given.

Mixture type	w/c ratio	Average splitting strength ± standard deviation (MPa)	Weibull modulus (m)	Scaling factor (σ_0, MPa)	R^2
Slag paste	0.3	29.82 ± 3.34	9.41	31.20	0.97
	0.4	21.78 ± 2.78	8.81	22.83	0.95
	0.5	17.89 ± 2.46	8.68	18.71	0.94
Portland cement paste [37]	0.3	21.28 ± 4.29	6.45	22.72	0.91
	0.4	18.72 ± 3.85	5.14	19.48	0.93
	0.5	16.54 ± 3.71	4.86	18.54	0.97

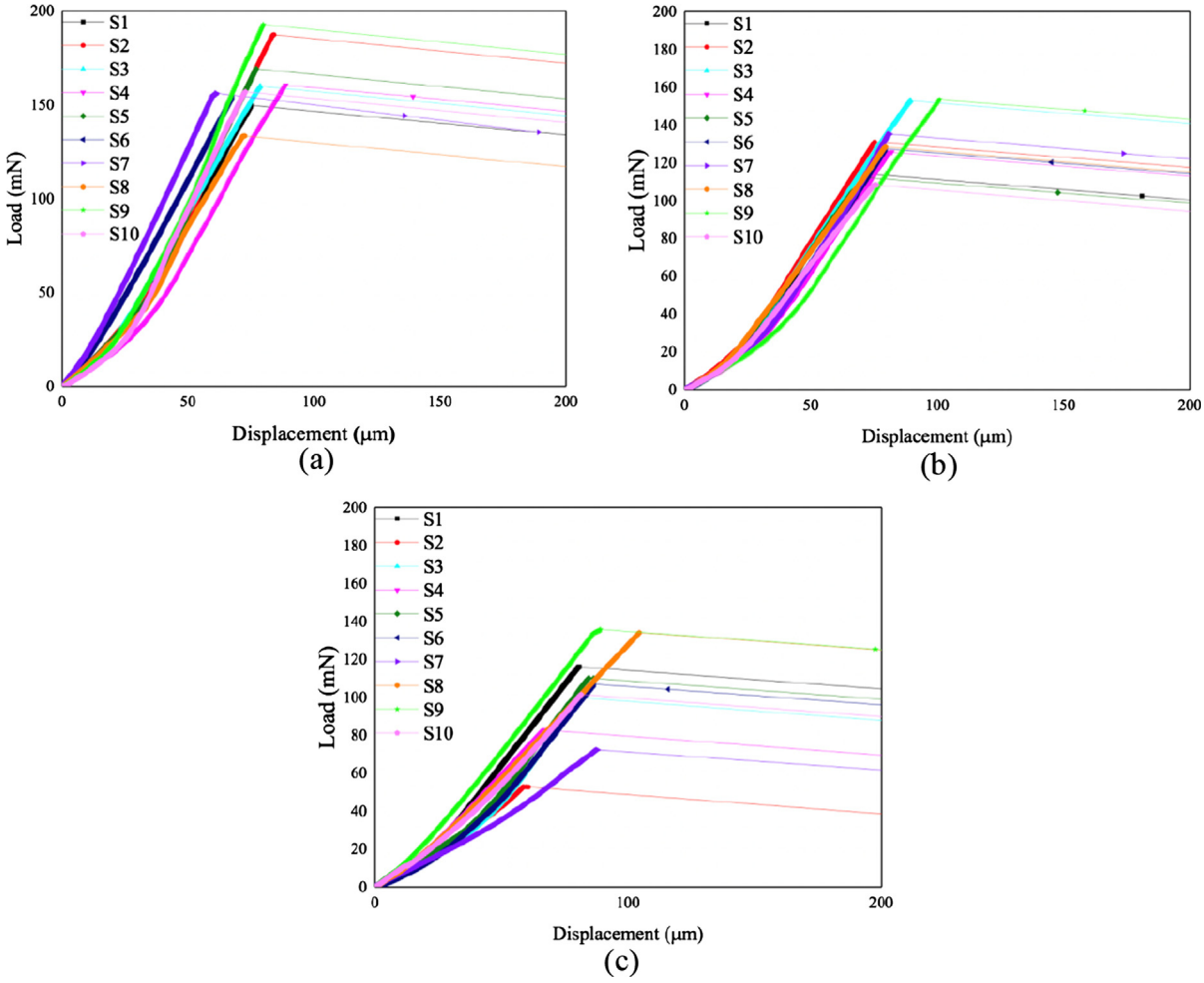

Fig. 14. Load vs. displacement curves of micro-beam specimens subjected to three-point bending. (a) w/c = 0.3; (b) w/c = 0.4; and (c) w/c = 0.5. Note that the post peak cannot be measured with this technique, so the data recorded after the peak load have no physical meaning.

Table 5
Young's modulus and flexural strength for the tested mixtures measured by micro-beam bending. For comparison, result of Portland cement paste specimens from our previous work are given.

Mixture type	W/c ratio	Young's modulus (GPa)	Flexural strength (MPa)
Slag paste	0.3	18.99 ± 2.27	23.32 ± 2.38
	0.4	13.95 ± 0.97	18.56 ± 2.11
	0.5	10.35 ± 2.03	14.57 ± 3.56
Portland cement paste [36]	0.3	16.68 ± 1.92	20.28 ± 2.63
	0.4	12.79 ± 2.13	15.31 ± 2.93
	0.5	9.09 ± 1.56	11.71 ± 2.22

cumulative histogram. It should be noted that only pores larger than the X-ray CT resolution can be detected in this manner, so the porosities are lower than those obtained using other methods. Nevertheless, the purpose here is to compare the values for different w/c ratios and cements. The results are given in Table 6.

It can be seen that CEM III/B pastes have lower porosity for all w/c ratios compared to CEM I pastes tested. This has an influence on both the tensile strength and the modulus. The largest difference between the two cement types is for the splitting strengths of pastes with w/c = 0.3 (Table 4). As described in our previous work [37], not all tested CEM I pastes could be split because at the time the maximum load was limited. Therefore, splitting strength of CEM I pastes with w/c = 0.3 is underestimated. At present however, we have acquired a high loading cell, so the measured strengths for CEM III/B is accurate. Note that, since this limitation did not apply for micro-beam bending specimens, the

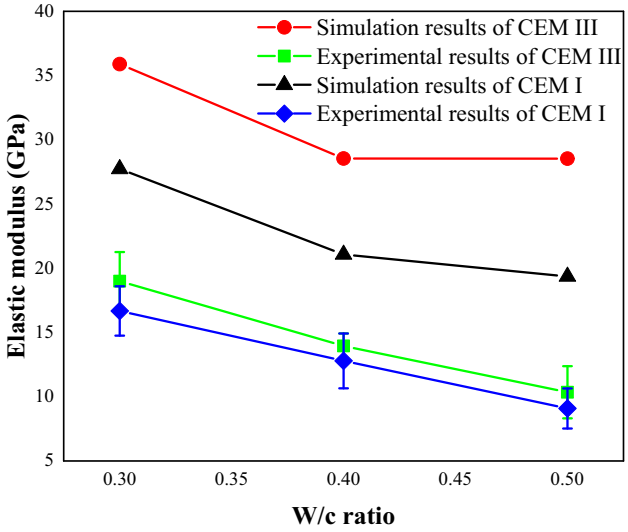

Fig. 15. A comparison between simulated and measured elastic moduli of cement pastes with different w/c ratios (error bars indicate standard deviation, modelling and experimental results for CEM I are taken from the authors' previous work [36,42]).

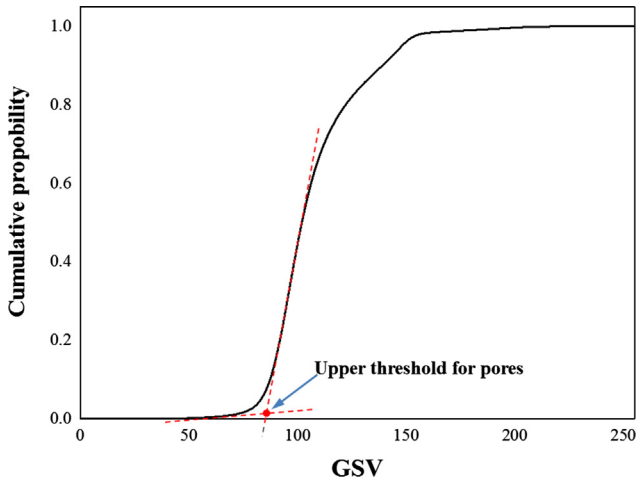

Fig. 16. Schematic explanation of the approach used to segment the capillary pores.

Table 6
Capillary porosity of cement pastes determined from X-ray CT images.

Mixture type	w/c ratio	Capillary porosity (%)
Slag paste	0.3	5.73
	0.4	7.89
	0.5	9.79
Portland cement paste [36]	0.3	8.44
	0.4	11.84
	0.5	17.5

difference in flexural strength of micro-beams with w/c = 0.3 (Table 5) is much smaller compared to the difference in splitting strength.

4. Conclusions

In this work, a modelling procedure for simulating deformation and fracture of cement pastes containing large amounts of blast furnace slag (CEM III/B) is presented and validated. A correlation between grayscale values resulting from X-ray CT scans of paste specimens and nanoindentation results, developed in our previous work, was exploited to create input for micromechanical models. Deformation and fracture of specimens with varying w/c ratio was simulated using the Delft lattice model. In addition, experiments were performed to validate the simulation outputs. Based on the presented results, the following conclusions can be drawn:

- Grayscale values from X-ray CT scans of slag pastes can be linearly correlated with nanoindentation measurements of elastic modulus. This can be used to create input for micromechanical models.
- Simulation results show that, for the same w/c ratio, slag pastes have higher tensile strength and elastic modulus compared to the Portland cement pastes at 28 days.
- Experimental measurements confirmed that tensile strength and elastic moduli of slag pastes at 28 days are higher than those of Portland cement pastes with the same w/c ratio. This is due to the lower capillary porosity, as confirmed by segmentation of X-ray CT images.
- Simulation results match the measured tensile strength quite well. Some discrepancy does exist at lower w/c ratios, possibly due to the assumptions made in the model.
- Simulated elastic moduli follow the same trend as the experiments, although measured values are always lower probably due to secondary experimental effects.

As stated in the introduction, not many works have been devoted to understanding of the micromechanical behavior of blended cement pastes, although they are increasingly used in practice. At present, their benefit is mostly seen in increasing the durability due to refinement of the pore structure. As shown herein, this effect causes difference in fracture behavior and strength at the micro-meter length scale. The presented work will form a basis for further investigations of these effects.

Acknowledgements

This work has been financially supported by an European Union Horizon 2020 project was sponsored by European Commission, European Union; InnovaConcrete (Innovative Materials and Techniques for the Conservation of 20th Century Concrete-Based Cultural Heritage), Grant Agreement Number 760858. Hongzhi Zhang would like to acknowledge the financial support of the China Scholarship Council, China; (CSC) under Grant CSC No. 201506120067. Arjan Thijssen performed the X-ray computed tomography experiments and his assistance is gratefully acknowledged.

References

[1] C. Chen, G. Habert, Y. Bouzidi, A. Jullien, Environmental impact of cement production: detail of the different processes and cement plant variability evaluation, J. Cleaner Prod. 18 (2010) 478–485.
[2] J.L. Provis, Geopolymers and other alkali activated materials: why, how, and what?, Mater. Struct. 47 (2014) 11–25.
[3] B. Lothenbach, K. Scrivener, R. Hooton, Supplementary cementitious materials, Cem. Concr. Res. 41 (2011) 1244–1256.
[4] R. Snellings, G. Mertens, J. Elsen, Supplementary cementitious materials, Rev. Mineral. Geochem. 74 (2012) 211–278.
[5] V. Baroghel-Bouny, K. Kinomura, M. Thiery, S. Moscardelli, Easy assessment of durability indicators for service life prediction or quality control of concretes with high volumes of supplementary cementitious materials, Cem. Concr. Compos. 33 (2011) 832–847.
[6] K. Lee, H. Lee, S. Lee, G. Kim, Autogenous shrinkage of concrete containing granulated blast-furnace slag, Cem. Concr. Res. 36 (2006) 1279–1285.
[7] S. Das, M. Aguayo, V. Dey, R. Kachala, B. Mobasher, G. Sant, N. Neithalath, The fracture response of blended formulations containing limestone powder: evaluations using two-parameter fracture model and digital image correlation, Cem. Concr. Compos. 53 (2014) 316–326.
[8] S. Das, M. Aguayo, G. Sant, B. Mobasher, N. Neithalath, Fracture process zone and tensile behavior of blended binders containing limestone powder, Cem. Concr. Res. 73 (2015) 51–62.
[9] J.G. Van Mier, Fracture processes of concrete, CRC press, 2017.
[10] G. Constantinides, F.-J. Ulm, The effect of two types of CSH on the elasticity of cement-based materials: results from nanoindentation and micromechanical modeling, Cem. Concr. Res. 34 (2004) 67–80.
[11] W. Zhu, J.J. Hughes, N. Bicanic, C.J. Pearce, Nanoindentation mapping of mechanical properties of cement paste and natural rocks, Mater. Charact. 58 (2007) 1189–1198.
[12] J.J. Hughes, P. Trtik, Micro-mechanical properties of cement paste measured by depth-sensing nanoindentation: a preliminary correlation of physical properties with phase type, Mater. Charact. 53 (2004) 223–231.
[13] D. Davydov, M. Jirásek, L. Kopecký, Critical aspects of nano-indentation technique in application to hardened cement paste, Cem. Concr. Res. 41 (2011) 20–29.
[14] S.J. Chen, W.H. Duan, Z.J. Li, T.B. Sui, New approach for characterisation of mechanical properties of cement paste at micrometre scale, Mater. Des. 87 (2015) 992–995.
[15] J. Němeček, V. Králík, V. Šmilauer, L. Polívka, A. Jäger, Tensile strength of hydrated cement paste phases assessed by micro-bending tests and nanoindentation, Cem. Concr. Compos. 73 (2016) 164–173.
[16] Y. Wei, X. Gao, S. Liang, Nanoindentation-based study of the micro-mechanical properties, structure, and hydration degree of slag-blended cementitious materials, J. Mater. Sci. 51 (2016) 3349–3361.
[17] V.Z. Zadeh, C.P. Bobko, Nanoscale mechanical properties of concrete containing blast furnace slag and fly ash before and after thermal damage, Cem. Concr. Compos. 37 (2013) 215–221.
[18] C. Hu, Z. Li, Y. Gao, Y. Han, Y. Zhang, Investigation on microstructures of cementitious composites incorporating slag, Adv. Cem. Res 26 (2014) 222–232.
[19] F. Pelisser, P.J.P. Gleize, A. Mikowski, Effect of the Ca/Si molar ratio on the micro/nanomechanical properties of synthetic CSH measured by nanoindentation, The Journal of Physical Chemistry C 116 (2012) 17219–17227.

[20] C. Hu, Z. Li, Property investigation of individual phases in cementitious composites containing silica fume and fly ash, Cem. Concr. Compos. 57 (2015) 17–26.
[21] C. Hu, Microstructure and mechanical properties of fly ash blended cement pastes, Constr. Build. Mater. 73 (2014) 618–625.
[22] W. Wilson, L. Sorelli, A. Tagnit-Hamou, Unveiling micro-chemo-mechanical properties of C–(A)–S–H and other phases in blended-cement pastes, Cem. Concr. Res. 107 (2018) 317–336.
[23] C. Hu, Z. Li, A review on the mechanical properties of cement-based materials measured by nanoindentation, Constr. Build. Mater. 90 (2015) 80–90.
[24] B. Pichler, C. Hellmich, Upscaling quasi-brittle strength of cement paste and mortar: a multi-scale engineering mechanics model, Cem. Concr. Res. 41 (2011) 467–476.
[25] J. Sanahuja, L. Dormieux, G. Chanvillard, Modelling elasticity of a hydrating cement paste, Cem. Concr. Res. 37 (2007) 1427–1439.
[26] M. Luković, E. Schlangen, G. Ye, Combined experimental and numerical study of fracture behaviour of cement paste at the microlevel, Cem. Concr. Res. 73 (2015) 123–135.
[27] M. Zhang, A.P. Jivkov, Microstructure-informed modelling of damage evolution in cement paste, Constr. Build. Mater. 66 (2014) 731–742.
[28] J.-S. Kim, S.-Y. Chung, D. Stephan, T.-S. Han, Issues on characterization of cement paste microstructures from μ-CT and virtual experiment framework for evaluating mechanical properties, Constr. Build. Mater. 202 (2019) 82–102.
[29] T.-S. Han, X. Zhang, J.-S. Kim, S.-Y. Chung, J.-H. Lim, C. Linder, Area of lineal-path function for describing the pore microstructures of cement paste and their relations to the mechanical properties simulated from μ-CT microstructures, Cem. Concr. Compos. 89 (2018) 1–17.
[30] M. Hlobil, V. Šmilauer, G. Chanvillard, Micromechanical multiscale fracture model for compressive strength of blended cement pastes, Cem. Concr. Res. 83 (2016) 188–202.
[31] F. Lavergne, A.B. Fraj, I. Bayane, J. Barthélémy, Estimating the mechanical properties of hydrating blended cementitious materials: an investigation based on micromechanics, Cem. Concr. Res. 104 (2018) 37–60.
[32] S. Bishnoi, K.L. Scrivener, μic: A new platform for modelling the hydration of cements, Cem. Concr. Res. 39 (2009) 266–274.
[33] G. Ye, K. Van Breugel, A. Fraaij, Three-dimensional microstructure analysis of numerically simulated cementitious materials, Cem. Concr. Res. 33 (2003) 215–222.
[34] P. Gao, Simulation of hydration and microstructure development of blended cements, Delft University of Technology PhD Thesis, Delft, The Netherlands, 2018.
[35] H. Zhang, B. Šavija, M. Luković, E. Schlangen, Experimentally informed micromechanical modelling of cement paste: an approach coupling X-ray computed tomography and statistical nanoindentation, Compos. B Eng. 157 (2019) 109–122.
[36] H. Zhang, B. Šavija, S.C. Figueiredo, E. Schlangen, Experimentally validated multi-scale modelling scheme of deformation and fracture of cement paste, Cem. Concr. Res. 102 (2017) 175–186.
[37] H. Zhang, B. Šavija, Y. Xu, E. Schlangen, Size effect on splitting strength of hardened cement paste: experimental and numerical study, Cem. Concr. Compos. 94 (2018) 264–276.
[38] B. Šavija, H. Zhang, E. Schlangen, Influence of Microencapsulated Phase Change Material (PCM) Addition on (Micro) Mechanical Properties of Cement Paste, Materials 10 (2017) 863.
[39] H. Zhang, B. Šavija, S. Chaves Figueiredo, M. Lukovic, E. Schlangen, Microscale Testing and Modelling of Cement Paste as Basis for Multi-Scale Modelling, Materials 9 (2016) 907.
[40] K. Scrivener, R. Snellings, B. Lothenbach, A practical guide to microstructural analysis of cementitious materials, Crc Press, 2018.
[41] M. Zhang, A.P. Jivkov, Micromechanical modelling of deformation and fracture of hydrating cement paste using X-ray computed tomography characterisation, Compos. B Eng. 88 (2016) 64–72.
[42] H. Zhang, B. Šavija, E. Schlangen, Towards understanding stochastic fracture performance of cement paste at micro length scale based on numerical simulation, Constr. Build. Mater. 183 (2018) 189–201.
[43] B. Šavija, H. Zhang, E. Schlangen, Assessing Hydrated Cement Paste Properties Using Experimentally Informed Discrete Models, J. Mater. Civ. Eng. 31 (2019) 04019169.
[44] H. Zhang, Y. Gan, Y. Xu, S. Zhang, E. Schlangen, B. Šavija, Experimentally informed fracture modelling of interfacial transition zone at micro-scale, Cem. Concr. Compos. 103383 (2019).
[45] M. Luković, B. Šavija, H. Dong, E. Schlangen, G. Ye, Micromechanical study of the interface properties in concrete repair systems, J. Adv. Concr. Technol. 12 (2014) 320–339.
[46] W.C. Oliver, G.M. Pharr, An improved technique for determining hardness and elastic modulus using load and displacement sensing indentation experiments, J. Mater. Res. 7 (1992) 1564–1583.
[47] J.J. Chen, L. Sorelli, M. Vandamme, F.J. Ulm, G. Chanvillard, A Coupled Nanoindentation/SEM-EDS Study on Low Water/Cement Ratio Portland Cement Paste: Evidence for C-S–H/Ca (OH) 2 Nanocomposites, J. Am. Ceram. Soc. 93 (2010) 1484–1493.
[48] K.J. Krakowiak, J.J. Thomas, S. Musso, S. James, A.-T. Akono, F.-J. Ulm, Nano-chemo-mechanical signature of conventional oil-well cement systems: effects of elevated temperature and curing time, Cem. Concr. Res. 67 (2015) 103–121.
[49] A. Deirieh, J. Ortega, F.-J. Ulm, Y. Abousleiman, Nanochemomechanical assessment of shale: a coupled WDS-indentation analysis, Acta Geotech. 7 (2012) 271–295.
[50] S. Monfared, H. Laubie, F. Radjai, M. Hubler, R. Pellenq, F.-J. Ulm, A methodology to calibrate and to validate effective solid potentials of heterogeneous porous media from computed tomography scans and laboratory-measured nanoindentation data, Acta Geotech. 13 (2018) 1369–1394.
[51] D. Phillips, J. Lannutti, Measuring physical density with X-ray computed tomography, NDT and E Int. 30 (1997) 339–350.
[52] N. Douarche, D. Rouby, G. Peix, J. Jouin, Relations between X-ray tomography, density and mechanical properties in carbon–carbon composites, Carbon 39 (2001) 1455–1465.
[53] F.J. Massey Jr, The Kolmogorov-Smirnov test for goodness of fit, J. Amer. Statistical Assoc. 46 (1951) 68–78.
[54] M.H. Gail, S.B. Green, Critical values for the one-sided two-sample Kolmogorov-Smirnov statistic, J. Amer. Statistical Assoc. 71 (1976) 757–760.
[55] B. Šavija, G. Smith, D. Liu, E. Schlangen, P. Flewitt, Modelling of deformation and fracture for a model quasi-brittle material with controlled porosity: Synthetic versus real microstructure, Eng. Fract. Mech. 205 (2019) 399–417.
[56] I. Stubna, P. Sin, P. Viljus, A. Trnik, The effect of firing temperature on the hardness of alumina porcelain, Mater. Technol. 48 (2014) 331–336.
[57] P. Zhang, S. Li, Z. Zhang, General relationship between strength and hardness, Mater. Sci. Eng., A 529 (2011) 62–73.
[58] H. Zhang, B. Šavija, E. Schlangen, Combined experimental and numerical study on micro-cube indentation splitting test of cement paste, Eng. Fract. Mech. (2018).
[59] E. Schlangen, E. Garboczi, Fracture simulations of concrete using lattice models: computational aspects, Eng. Fract. Mech. 57 (1997) 319–332.
[60] E. Schlangen, Z. Qian, 3D modeling of fracture in cement-based materials, Journal of Multiscale Modelling 1 (2009) 245–261.
[61] M. Luković, H. Dong, B. Šavija, E. Schlangen, G. Ye, K. van Breugel, Tailoring strain-hardening cementitious composite repair systems through numerical experimentation, Cem. Concr. Compos. 53 (2014) 200–213.
[62] M. Nooru-Mohamed, E. Schlangen, J.G. van Mier, Experimental and numerical study on the behavior of concrete subjected to biaxial tension and shear, Adv. Cem. Based Mater. 1 (1993) 22–37.
[63] E. Schlangen, E. Koenders, K. Van Breugel, Influence of internal dilation on the fracture behaviour of multi-phase materials, Eng. Fract. Mech. 74 (2007) 18–33.
[64] M. Luković, B. Šavija, E. Schlangen, G. Ye, K. van Breugel, A 3D lattice modelling study of drying shrinkage damage in concrete repair systems, Materials 9 (2016) 575.
[65] Z. Qian, E. Schlangen, G. Ye, K. van Breugel, Modeling Framework for Fracture in Multiscale Cement-Based Material Structures, Materials 10 (2017) 587.
[66] M. Yip, J. Mohle, J. Bolander, Automated Modeling of Three-Dimensional Structural Components Using Irregular Lattices, Comput.-Aided Civ. Infrastruct. Eng. 20 (2005) 393–407.
[67] B. Šavija, D. Liu, G. Smith, K.R. Hallam, E. Schlangen, P.E. Flewitt, Experimentally informed multi-scale modelling of mechanical properties of quasi-brittle nuclear graphite, Eng. Fract. Mech. 153 (2016) 360–377.
[68] C. Castellano, V. Bonavetti, H. Donza, E. Irassar, The effect of w/b and temperature on the hydration and strength of blastfurnace slag cements, Constr. Build. Mater. 111 (2016) 679–688.
[69] M. Öner, K. Erdoğdu, A. Günlü, Effect of components fineness on strength of blast furnace slag cement, Cem. Concr. Res. 33 (2003) 463–469.
[70] Z. Li, Z. Ding, Property improvement of Portland cement by incorporating with metakaolin and slag, Cem. Concr. Res. 33 (2003) 579–584.
[71] D. Liu, B. Šavija, G.E. Smith, P.E. Flewitt, T. Lowe, E. Schlangen, Towards understanding the influence of porosity on mechanical and fracture behaviour of quasi-brittle materials: experiments and modelling, Int. J. Fract. 205 (2017) 57–72.
[72] J.G. Van Mier, Fracture processes of concrete, CRC press1997.
[73] J.B. Quinn, G.D. Quinn, A practical and systematic review of Weibull statistics for reporting strengths of dental materials, Dent. Mater. 26 (2010) 135–147.
[74] P. Pizette, C. Martin, G. Delette, P. Sornay, F. Sans, Compaction of aggregated ceramic powders: From contact laws to fracture and yield surfaces, Powder Technol. 198 (2010) 240–250.
[75] J. Birchall, A. Howard, K. Kendall, Flexural strength and porosity of cements, Nature 289 (1981) 388.
[76] K.L. Scrivener, Backscattered electron imaging of cementitious microstructures: understanding and quantification, Cem. Concr. Compos. 26 (2004) 935–945.